Engineering Geology 237 (2018) 76–91

Contents lists available at ScienceDirect

Engineering Geology

journal homepage: www.elsevier.com/locate/enggeo

Probabilistic liquefaction-induced lateral spread hazard mapping and its application to Utah County, Utah

Mahyar Sharifi-Mood[a,*], Daniel T. Gillins[b], Kevin W. Franke[c], Jasmyn N. Harper[d], Steven J. Bartlett[e], Michael J. Olsen[f]

[a] Department of Civil, Architectural, and Environmental Engineering, University of Texas, Austin, TX 78712, USA
[b] National Geodetic Survey, National Oceanic and Atmospheric Administration, 1315 East-West Highway, Silver Spring, MD 20910, USA
[c] Department of Civil and Environmental Engineering, Brigham Young Univ., Provo, UT 84602, USA
[d] FM Global, 601 108th Ave NE, Ste 1400, Bellevue, WA 98004, USA
[e] Department of Civil and Environmental Engineering, University of Utah, 122 S. Central Campus Dr., Salt Lake City, UT 84112, USA
[f] School of Civil and Construction Engineering, Oregon State University, Corvallis, OR 97331 3212, USA

ARTICLE INFO

Keywords:
Lateral spread displacement
Probabilistic
Liquefaction
Hazard mapping
Uncertainty modeling
Performance-based

ABSTRACT

Earthquake-induced liquefaction may result in the lateral spread displacement of soil down gently sloping ground or towards a free-face, causing severe and costly damage to various facilities, bridges, buildings and other critical infrastructure. Despite the availability of analytical methods, most engineers currently use empirical or semi-empirical regression models to estimate liquefaction-induced lateral spread displacements at specific sites. However, the application of these regression models for regional mapping over a large geographic areas can be difficult because of challenges associated with the adequate characterization of subsurface soil and groundwater conditions, geotechnical properties, regional topography, and uncertainties associated with the causative seismic loading. To address these challenges, this paper presents a new and fully probabilistic procedure for regional hazard mapping of liquefaction-induced lateral spread displacement. The mapping process is demonstrated through an implementation in Utah County, Utah. To demonstrate the type of lateral spread displacement hazard maps possible, maps corresponding to return periods of 1033 and 2475 years are developed for Utah County, Utah. The proposed procedure incorporates topographical data from airborne lidar surveys and geotechnical and geological data from available maps and subsurface explorations. It accounts for uncertainties in the soil properties, seismic loading, and the empirical models for predicting lateral spread displacement using Monte Carlo simulations.

1. Introduction

Seismically-induced soil liquefaction occurs as excess pore water pressure generated by cyclic strains in loose, saturated, and cohesionless soil significantly reduces the shear resistance and stiffness of the soil. A horizontal movement in the soil above a liquefied subsurface layer is called lateral spread (Youd et al., 2001). This type of movement generally develops on gently sloping ground or in the vicinity of a free-face (e.g., river channels, canals or abrupt topographical depression). Lateral spreads have historically resulted in excessive cost and damage to urban communities by rupturing utility lines, destroying foundations, and straining structures. Recent major earthquakes in New Zealand, Japan, Peru, Chile, China, and Haiti have highlighted the need for earthquake engineers to be able to assess, delineate, and quantify the potential for lateral spread hazard when evaluating both new and existing facilities on loose soil sites.

Geotechnical engineers most commonly evaluate liquefaction and lateral spread hazard either analytically or empirically using site-specific techniques. However, some researchers have attempted to quantify and map liquefaction and ground displacement hazard across a larger region (such as a county) in an effort to produce preliminary hazard evaluation for planning, engineering and development purposes. Early liquefaction hazard mapping efforts were generally qualitative and based largely on liquefaction susceptibility correlations with mapped surficial geology. These were implemented out of necessity due to insufficient subsurface soil and groundwater information, or lack of development of predictive models that incorporated important site and soil factors (e.g., Youd and Hoose, 1977; Youd and Perkins, 1978). Later, liquefaction potential mapping efforts (e.g., Anderson et al., 1982; Baise et al., 2006) began considering regional seismic loading in

* Corresponding author at: Advanced Computing Building, 10505 Exploration Way, Austin, TX 78758, USA.
E-mail address: mahyar.sh@utexas.edu (M. Sharifi-Mood).

https://doi.org/10.1016/j.enggeo.2018.01.015
Received 18 August 2017; Received in revised form 14 December 2017; Accepted 20 January 2018
Available online 27 February 2018
0013-7952/

addition to liquefaction susceptibility correlations with mapped surface geology to characterize the regional liquefaction triggering hazard. The additional evaluation of the available subsurface geotechnical information across a region in the liquefaction hazard mapping process (e.g., Anderson et al., 1982; Baise et al., 2006; Lenz and Baise, 2007; Olsen et al., 2007; Gillins, 2012) improved the characterization of the liquefaction triggering hazard. These approaches typically used the results for the "critical layer" (i.e., the layer of soil with the smallest factor of safety against liquefaction triggering) in the soil profile to define the liquefaction hazard. However, other researchers have quantified this hazard using a different metric such as liquefaction potential index (LPI) (e.g., Iwasaki et al., 1982; Luna and Frost, 1998; Holzer et al., 2006; Cramer et al., 2008), liquefaction risk index (LRI) (e.g., Lee et al., 2004; Sonmez and Gokceoglu, 2005) or liquefaction severity index (LSI) (e.g., Youd and Perkins, 1987). Each of these indices are calculated by integrating the liquefaction triggering potential across all potentially liquefiable soil layers at a site to a single value.

While integrated liquefaction hazard metrics such as LPI, LSI and LRI have proven useful in mapping the liquefaction triggering hazard across a region, they have been shown to correlate rather poorly with observed lateral spread displacements following major earthquake events because of other relevant factors such as site topography and spatial continuity that are not accounted for in their computation (Maurer et al., 2014; Rashidian and Gillins, 2018). Other investigators have developed lateral spread displacement hazard maps using correlations with mapped surface geology (e.g., Youd and Perkins, 1978) or empirical displacement prediction models in the mapping procedure (e.g., Mabey and Madin, 1993; Olsen et al., 2007; Gillins, 2012; Jaimes et al., 2015; Sharifi-Mood et al., 2017b). These latter displacement hazard maps were developed from a single earthquake scenario developed from either a deterministic seismic hazard analysis or a probabilistic seismic hazard analysis at a single return period. However, these maps do not consider seismic loading from multiple seismic sources and across multiple return periods, nor do they account for variation in ground motion amplification from site response effects (e.g., Bazzurro and Cornell, 2004; Stewart et al., 2014).

This study presents a new and comprehensive procedure to develop fully probabilistic lateral spread hazard prediction maps that account for uncertainties in ground motions, site response, subsurface geotechnical and groundwater information, and lateral spread displacement prediction models. This procedure is based on a performance-based earthquake engineering framework that incorporates probabilistic seismic hazard analysis (PSHA) of the region, site geology base maps, available subsurface geotechnical investigations, available groundwater data, and high-resolution light detection and ranging (lidar) topographic data. The proposed methodology is demonstrated for a study area in Utah County, Utah, resulting in probabilistic lateral spread displacement hazard maps for the area corresponding to the return periods of 1033 and 2475 years.

2. Prediction of lateral spread displacements

Currently, lateral spread displacement prediction methods can be divided into three generalized categories (Franke, 2005): (1) empirical prediction models based solely on field data and observation (e.g., Hamada et al., 1986; Bartlett and Youd, 1995; Rauch and Martin, 2000; Bardet et al., 2002; Youd et al., 2002; Gillins and Bartlett, 2013); (2) semi-empirical prediction models based on theoretical derivation that are calibrated against laboratory and/or field data (e.g., Zhang et al., 2004; Faris et al., 2006; Idriss and Boulanger, 2008); and (3) analytical prediction models that numerically compute displacements and that are based on the mechanics of the liquefaction and/or horizontal ground deformation (e.g., Bray and Travasarou, 2007; Seid-Karbasi and Byrne, 2007; Saygili and Rathje, 2008; Lam et al., 2009). Despite the fact that analytical methods continue to make significant progress in their ability to accurately predict lateral spread displacements, empirical and semi-empirical prediction models remain the most popular method for predicting lateral spread displacements among engineering practitioners today because of their simplicity, familiarity, and basis in field performance from case histories of lateral spread (Franke and Kramer, 2014). However, a large amount of aleatory uncertainty is usually associated with these types of predictive models, or in fact with any type predictive model, because of the complexities of the subsurface geology and lateral spread phenomenon and the paucity of well-documented lateral spread case histories for developing robust empirical models.

Bartlett and Youd (1995) originally considered lateral spread events from earthquakes in Japan and the western United States and statistically regressed an empirical prediction model from their resulting case history data that included earthquake moment magnitude, source-to-site distance, several geotechnical soil factors, and slope geometry. Later, Youd et al. (2002) updated their lateral spread case history database and developed a revised multilinear regression prediction model, which remains widely used by engineering practitioners today. Recently, Gillins and Bartlett (2013) simplified the Youd et al. (2002) prediction model by consolidating some of the required geotechnical input factors such as fines content and mean grain size into a single soil classification factor. The Gillins and Bartlett (2013) model was developed specifically for lateral spread hazard mapping applications because it does not require laboratory test results for the soil but instead relies upon visual soil classifications, which are more readily available in most geotechnical field boring logs. The Gillins and Bartlett (2013) multilinear regression empirical model is given as:

$$\log D_H = b_0 + b_1 M_W + b_2 Log\ R^* + b_3 R + b_4 Log\ W + b_5 Log\ S + b_6 Log\ T_{15,cs} + 0.252 + \varepsilon \quad (1)$$

where D_H is the permanent estimated horizontal lateral spread displacement in meters; M_W is the moment magnitude of the earthquake; R is the closest horizontal distance in kilometers from the site to the vertical surface projection of the fault rupture (i.e., the Joyner-Boore distance, R_{JB}); W is the free-face ratio (i.e., the ratio of the height to the horizontal distance from the site to the toe of the slope) in percent (%); S is the slope gradient in percent (%); and R^* is a distance parameter used to characterize near-source earthquakes and is computed as:

$$R^* = R + 10^{0.89 M_W - 5.64} \quad (2)$$

$T_{15,\ cs}$, which is the only geotechnical variable in Eq. (1), is the clean-sand equivalent value for T_{15}, and is computed as:

$$T_{15,cs} = T_{15}.\ 10^{\left(\frac{-0.683\,x_1 - 0.200\,x_2 + 0.252\,x_3 - 0.040\,x_4 - 0.535\,x_5 - 0.252}{0.592}\right)} \quad (3)$$

where T_{15} is the cumulative thickness (in meters) of saturated, cohesionless, and continuous soil deposits in the upper 15 m of the soil profile with corrected standard penetration test (SPT) $(N_1)_{60} < 15$ hammer blows per 0.3 m, and x_n is the ratio of the cumulative thickness (in meters) of soil with a Soil Index (SI) value n with $(N_1)_{60} < 15$ to the total T_{15} for the entire soil column. Thus, x_n will range between 0 and 1, and the sum of x_1 through x_5 will equal 1. SI values and their definitions are provided in Table 1.

Using the Youd et al. (2002) lateral spread case history database, Gillins and Bartlett (2013) solved for the regression coefficients, b_0 to b_6, for Eq. (3). These coefficients are given in Table 2 according to the

Table 1
Soil Index (SI) values and their definitions (from Gillins, 2012).

SI	Definition
1	Silty gravel with sand, silty gravel, fine gravel
2	Coarse to very coarse sand, sand and gravel, gravelly sand
3	Sand, medium to fine sand, sand with some silt
4	Fine to very fine sand, sand with silt, silty sand, dirty sand
5	Sandy silt, silt with sand
6	Non-liquefiable, such as cohesive soil or soil with high plasticity

Table 2
Gillins and Bartlett (2013) empirical regression model coefficients for lateral spread displacement prediction.

Model	b_0	b_1	b_2	b_3	b_4	b_5	b_6
Ground - slope	−8.208	1.318	−1.073	−0.016	0	0.337	0.592
Free face	−8.552	1.318	−1.073	−0.016	0.445	0	0.592

topographic conditions at a site. The error for the regression model, ε, is normally distributed with a mean of 0.0 and a standard deviation, $\sigma_{log_{DH}} = 0.2232$ and the coefficient of determination, R^2 is 79.0%.

3. Performance-based prediction of lateral spread displacements

Earthquake scientists and engineers have long recognized that many uncertainties exist associated with predicting earthquake ground motions and their subsequent effects on the ground and structures. In response, these professionals have developed and implemented probabilistic or performance-based earthquake engineering design procedures, which quantify and account for as many of the uncertainties associated with the evaluation as possible. These procedures typically quantify the associated hazard in terms of a mean annual rate of exceedance, λ.

Franke and Kramer (2014) introduced a performance-based procedure built upon the probabilistic framework introduced by the Pacific Earthquake Engineering Research Center (PEER; Cornell and Krawinkler, 2000; Deierlein et al., 2003) to compute the mean annual rate of exceeding some lateral spread displacement, *d*. Their procedure modifies the Youd et al. (2002) model by grouping together all of the model variables related to seismic loading (i.e., M_W and R) and designating them as the apparent loading parameter, $\mathscr{L}$. Because $\mathscr{L}$ is a function of parameters M_W and R, it is analogous to a ground motion attenuation relationship and can be treated in a similar manner. Likewise, the Franke and Kramer procedure groups together all of the model variables related to local site conditions (i.e., S, W, T_{15}, fines content, and mean grain size) and designates them as a site parameter, G.

A similar modification can be applied to the Gillins and Bartlett (2013) model presented in Eq. (1). In this modified form of the model, the apparent loading parameter is defined as:

$$\mathscr{L} = b_1 M_W + b_2 Log\ R^* + b_3 R \tag{4}$$

The modified site parameter is defined as:

$$G = -(b_0 + b_4 Log\ W + b_5 Log\ S + b_6 Log\ T_{15,cs} + 0.252) \tag{5}$$

The model error is defined as:

$$\varepsilon = \sigma_{log_{D_H}} \Phi^{-1}[P] \tag{6}$$

where Φ^{-1} is the inverse standard normal cumulative distribution function, and P is the probability of exceeding the median predicted lateral spread displacement, $\widehat{D}_H$. Using this modified syntax, Eq. (1) can be re-written as:

$$\log D_H = \mathscr{L} - G + \varepsilon \tag{7}$$

As demonstrated by Franke and Kramer (2014), the modified lateral spread model can now be inserted into a performance-based framework to compute the mean annual rate of exceeding a specific lateral spread displacement *d* as:

$$\lambda_d = \sum_{i=1}^{N_{\mathscr{L}}} P[D_H > d \mid G, \mathscr{L}_i] \Delta\lambda_{\mathscr{L}_i} \tag{8}$$

where $N_{\mathscr{L}}$ is the number of bins or increments associated with the seismic hazard curve for $\mathscr{L}$ developed through a probabilistic seismic hazard analysis (PSHA); $\Delta\lambda_{\mathscr{L}_i}$ is the size of each hazard increment or bin associated with the seismic hazard curve for $\mathscr{L}$; and $P[D_H > d \mid G, \mathscr{L}_i]$ is the conditional probability that the median predicted lateral spread displacement exceeds displacement *d* conditional upon seismic loading $\mathscr{L}_i$ and constant site conditions G. If the model error term, ε, is removed or neglected, Eq. (1) will produce the mean value of $\log D_H$ (i.e., $\overline{\log D_H}$), and the conditional probability term shown in Eq. (8) can be computed as:

$$P[D_H > d \mid G, \mathscr{L}_i] = 1 - \Phi\left[\frac{\log d - \overline{\log D_H}}{\sigma_{log_{D_H}}}\right] = 1 - \Phi\left[\frac{\log d - \overline{\log D_H}}{0.2232}\right] \tag{9}$$

One of the advantages of the Franke and Kramer (2014) formulation of an empirical lateral spread model is that it distinguishes the seismic loading from the site parameters in the calculation of lateral spread displacement. By doing so, the procedure allows for $\mathscr{L}$ to be evaluated in a PSHA before any site-specific geotechnical or topographic information is available, thus resulting in a seismic hazard curve for $\mathscr{L}$. If all of the uncertainty from the lateral spread prediction (i.e., $\sigma_{log_{DH}}$) is assigned to $\mathscr{L}$ in the PSHA, then site-specific and probabilistic estimates of lateral spread displacement can be immediately computed once geotechnical and topographic information from the site become available.

Given that a seismic hazard curve for $\mathscr{L}$ can be developed for a given site through a PSHA that incorporates Eq. (4) before any site-specific soil and/or topographic information is available, it is then possible to develop a series of hazard curves for $\mathscr{L}$ across a geographic grid of points for the purpose of lateral spread displacement hazard mapping. Because the development of the $\mathscr{L}$ hazard curve is computationally expensive, the grid spacing at which the hazard curves are developed should be carefully considered. Ulmer et al. (2015) evaluated this problem and recommended grid spacing for the mapping of lateral spread displacement hazard as a function of mapped probabilistic values of peak ground acceleration (PGA) at a return period 2475 years from the U.S. Geological Survey (USGS) National Seismic Hazard Mapping Project (NSHMP). If PGA values at this return period exceed 0.64 g, then Ulmer et al. (2015) recommend a minimum grid spacing of 4 km.

4. Correlation of regional geotechnical properties to mapped surface geology

Eqs. (8) and (9) provide a performance-based framework to compute the mean annual rate of exceeding a particular lateral spread displacement, *d*, given a site geometry, *G*. Unfortunately, when mapping lateral spread displacement across a regional area using only available geotechnical data, *G* is highly uncertain due to the paucity of geotechnical drilling, sampling, and testing across the area. Since this problem often occurs in practice, this paper assumes there is generally a lack of available data to be able to spatially interpret geotechnical variables or develop a continuous ground water table model through a highly dense number of subsurface investigations, like done in other hazard mapping methods for smaller study areas (e.g., Liu et al., 2016; Juang et al., 2017; Baker and Faber, 2008; Chen et al., 2016). To deal with this problem and account for the high uncertainty in *G* across the region area of interest with limited geotechnical investigations, Monte Carlo simulations can be used to develop a range of $T_{15,\ cs}$ for given geologic units.

Sharifi-Mood (2017a) describes a procedure in which subsurface geotechnical exploration data and groundwater levels can be collected across the regional area of interest and correlated to mapped surface geology. SPT boring logs and CPT soundings can be collected from publicly available sources, as well as solicited from private consultants and owners, to develop a geotechnical subsurface database for the area. These subsurface explorations can then be grouped according to mapped surface geology within the database. For a given geologic unit, all logged soil properties for each *SI* defined in Table 1 are gathered together, and histograms and corresponding probability density functions (PDFs) are developed for each available or measured soil property

including unit weight, moisture content, and Atterberg limits. By thus grouping together the soils from each geologic unit and developing histograms for the available soil properties based on *SI* type, a Monte Carlo simulation can be used in the performance-based lateral spread hazard mapping procedure to randomly generate a soil profile and groundwater level that is consistent with any particular geologic unit of interest. The application of such a Monte Carlo simulation will be described in greater detail below.

Some discussion is warranted regarding the validity and applicability of correlating geotechnical properties to mapped surface geology. An ideal geotechnical sampling scheme for this type of approach would involve selecting a sufficient number of geotechnical explorations in each mapped geologic unit and spacing them sufficiently to capture the spatial uncertainty of the soil deposits within each geologic unit, particularly the "critical" liquefying soil deposit(s) that governs lateral spread behavior. Unfortunately, planning and implementing such a sampling scheme for the purpose of liquefaction and/or lateral spread displacement hazard mapping constitutes a significant effort and financial cost, and is therefore unfeasible for most researchers. Instead, most researchers must rely upon that geotechnical exploration data that is already available to them through public records and/or donation by private owners. As such, reliance upon such geotechnical exploration data is certain to result in the under-sampling of certain geologic units and geographic areas, the spatial clustering of geotechnical explorations along various infrastructure features such as highways, and an elevated risk of inconsistent and/or incorrect soil logging. Such paucity of data and inconsistency in sampling strategies also makes it difficult to spatially interpolate the data between investigations. However, given that liquefaction and lateral spread hazard maps are intended to be a preliminary assessment tool for engineers and decision-makers, and in no way are intended to supersede or replace site-specific liquefaction hazard analysis, such short-comings of the geotechnical database are both understandable and necessary.

5. Proposed performance-based lateral spread hazard mapping procedure

The proposed performance-based lateral spread hazard mapping procedure requires several inputs related to seismic loading, surface topography, and subsurface geotechnical properties across the region of interest. Most of these inputs come in the form of a digital raster, which consists of a matrix of pixels organized into rows and columns where each pixel contains a value representing information. The inputs required for the performance-based lateral spread hazard mapping procedure are as follows: (1) a raster of the mapped surface geology of the study area; (2) rasters of the ground slope and free-face ratios computed from a high-resolution digital elevation model (DEM); (3) a geotechnical database comprised of as many SPT logs and CPT soundings from as many of the mapped geologic units in the study area as possible; and (4) rasters of the seismic hazard curves for $\mathscr{L}$, developed from a series of PSHAs performed across the study area. The incorporation of these inputs for the development of performance-based lateral spread displacement hazard mapping procedure is illustrated in a flow chart diagram in Fig. 1. Each step of this flow chart is briefly summarized below.

For the proposed mapping procedure summarized in Fig. 1, the lateral spread hazard is computed for each individual pixel of a raster of the study area. The process is repeated for each pixel, and the results at each pixel are then combined to produce the final hazard maps. To accelerate the computations, the pixels can be evaluated simultaneously using parallel processing. However, for clarity, this paper will describe the process as if solving for the hazard at each pixel sequentially.

5.1. Step 1: extract raster data at a map pixel

Because the geology and depositional environment significantly influences the susceptibility of the soil to liquefaction, the proposed mapping method begins by utilizing available surface geology maps. These maps are compiled, digitized, georeferenced, and converted into a raster image for the mapping area.

In addition to developing a raster image of the surface geology of the mapping area, additional rasters are developed to describe the spatial variation in site geometry in the mapping area. Using a DEM, raster images of the percent ground slope, and proximity and depth of free-faces are computed (note that an example of computing these rasters is given in the following section).

For the proposed mapping method, the lateral spread hazard is computed for each individual pixel of a raster in the mapping area. As illustrated in Fig. 1, beginning at one pixel in the mapping area, the raster values from the surface geology, slope (S), and free-face (W) rasters are extracted at that location.

5.2. Step 2: begin Monte Carlo simulations, compute $T_{15,cs,i}$

Step 2 initiates a Monte Carlo simulation to account for uncertainty in the geotechnical properties and seismic loading at the pixel of interest. Given the mapped surface geologic unit for a given pixel being analyzed, a random geotechnical exploration (i.e., SPT log) is selected from the geotechnical database according to the mapped geologic unit. Soil properties that are missing or are not specified on the randomly selected log or sounding are randomly created from the histograms developed as part of the geotechnical database. While soil factors such as moisture content, fines content, Atterberg limits and dry unit weights are simulated, neither SPT N values nor soil types are simulated because only geotechnical explorations with these data listed with depth are used. Once a complete soil profile is available with SPT N values, soil layering with descriptions, and moisture content, fines content, dry unit weights, and Atterberg limits for each layer, then total and effective stress profiles are computed and the SPT N values are corrected to $(N_1)_{60}$ values. Then, a value for *SI* is assigned to each layer in the soil profile and a value of $T_{15,\ cs}$ is computed using Eq. (3). For an example of how to compute $T_{15,\ cs}$ from an SPT log, refer to Gillins and Bartlett (2013).

As part of this step, the procedure could be developed so that the random selection of an SPT for each Monte Carlo simulation is weighted based on the distance of the pixel of interest to the location of the available SPTs in the geotechnical database. A higher weight for random sampling could be given to nearer SPTs, since the soil profile is likely to be similar to the profile from nearby SPT(s). This approach would also ensure that if the pixel is located at the location of an SPT in the database, it uses the soil log from this SPT. Gillins (2012) developed a semivariogram of $T_{15,\ cs}$ for all boreholes in a geotechnical database and used this semivariogram as a basis for developing a weighting scheme. However, the semivariogram reached a sill at only 30 m. Thus, the pixel must be very close to an SPT for spatial correlation with its measured value for $T_{15,\ cs}$.

The computed value of $T_{15,\ cs}$ is then assigned to the i-th iteration of the Monte Carlo simulation as $T_{15,\ cs,\ i}$, and it is used in later steps to compute the corresponding lateral spread displacement for the i-th iteration. $T_{15,\ cs,\ i}$ is then combined with topographic parameters S and W associated with the pixel of interest and that were obtained in Step 1, and values of G_i are computed for both the free face and ground-slope conditions using Eq. (5) and Table 2.

5.3. Step 3: develop apparent loading parameter value, $\mathscr{L}_i$

Continuing with the i-th simulation, Step 3 randomly selects an apparent loading parameter value based on its corresponding likelihood. For each pixel, the corresponding hazard curve for $\mathscr{L}$ is first transformed to a PDF using the procedure presented by Bazzurro and Cornell (2004). A value of $\mathscr{L}$ is then randomly selected from the PDF according to its relative likelihood and is combined with G_i from Step 2

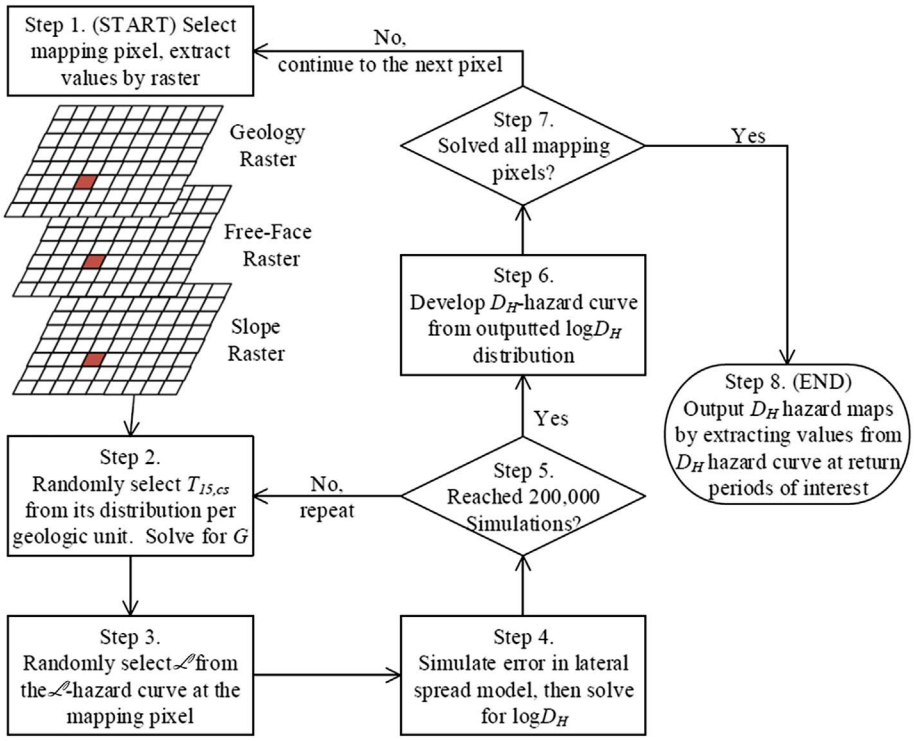

Fig. 1. Proposed procedure for producing performance-based lateral spread displacement hazard maps.

for the computation of logD_H.

The description above assumes that the series of PSHAs performed across the study area computes hazard curves for $\mathscr{L}$ at every pixel in mapping raster. However, the raster pixel spacing for mapping is commonly much smaller (e.g., 30 m) than the grid spacing for regional PSHA $\mathscr{L}$ due to the extensive number of calculations the PSHA typically requires. If such is the case, then an interpolation scheme must be performed to develop hazard curves of $\mathscr{L}$ for each pixel in the raster. Under this condition, a hazard curve for $\mathscr{L}$ can be derived through bilinear interpolation of the nearest gridded $\mathscr{L}$ hazard curves surrounding the pixel of interest.

5.4. Step 4: compute log D_H

The final step in i-th iteration of the Monte Carlo simulation is to solve Eq. (7). The subtracting G_i from Step 2 from the selected value for $\mathscr{L}_i$ from Step 3 produces $\overline{\log D_{H\,i}}$ for the iteration. A value for the error in the lateral spread displacement model, ε, is then simulated using a random number generator that follows the standard normal distribution.

Eq. (7) can now be rewritten to compute $[logD_H]_i$ for the i-th iteration at a mapping pixel as:

$$[\log D_H]_i = \overline{\log D_{H\,i}} + \varepsilon = \overline{\log D_{H\,i}} + \sigma_{\log_{D_H}} \cdot K_{rand,i} = \overline{\log D_{H\,i}} + 0.2232\, K_{rand,i} \quad (10)$$

where $K_{rand,\,i}$ is a random value generated from the standard normal distribution for the i-th simulation.

5.5. Step 5: repeat steps 2–4 for required number of simulations

Step 5 involves repeating Steps 2 through 4 until a full probability distribution of $[logD_H]$ is developed at the selected pixel. Development of a full probability distribution requires that an adequate number of iterations must be performed to fully characterize the major sources of uncertainty in the process. We observed that 200,000 simulations is generally sufficient to develop an adequate probability distribution of $[logD_H]$ at each pixel. Upon completion of all of the simulations, the probability distribution for $[logD_H]$ is transformed to a probability distribution for D_H values (in meters) for each pixel by raising each $[logD_H]$ value by the power of 10.

5.6. Step 6: develop a D_H hazard curve

In Step 6, the probability distribution for D_H is transformed into a hazard curve for D_H at each pixel. The probability distribution for D_H is first transformed into a cumulative distribution function (CDF) for D_H through numerical integration. Then using the Poisson probability model, the mean annual rate of exceeding some lateral spread displacement d (i.e., λ_d) is computed as:

$$\lambda_d = -\frac{\ln[1 - F(d)]}{t = 1} = -\ln[1 - F(d)] \quad (11)$$

where t is exposure period in years and is equal to unity to solve for the mean annual rate of exceedance, and $F(d)$ is the CDF function corresponding to the displacement d.

5.7. Step 7: repeat previous steps for all mapping pixels

Each of the first six steps are repeated for every pixel in the study area, resulting in hazard curves for D_H at every pixel.

5.8. Step 8: output maps for desired return periods

In Step 8, values of D_H are extracted from the hazard curves at a user-defined return period (e.g., 475, 1033, or 2475 years [10%, 5% and 2% in 50 years]) for each mapping pixel. The extracted value at each pixel can be aggregated into a raster image, and this image is then used to develop a lateral spread displacement hazard map at the desired return period.

6. Implementation of the mapping method for Utah County, Utah

As an example to clarify the proposed mapping method, the flow

chart illustrated in Fig. 1 was followed to produce lateral spread displacement hazard maps for Utah County, Utah. Utah County is the second-most populous county in the state of Utah and comprises a significant portion of the overall state and regional economies. However, the liquefaction hazard is considered significant in that portion of the county due to its close proximity to high seismic (e.g., the Wasatch fault) and surficial water (e.g., Utah Lake) sources, shallow ground water tables, and widespread granular and/or silty soils in the upper 5 to 15 m of sediments. Development of fully probabilistic liquefaction-induced lateral spread displacement hazard maps for the county will provide a tool for agencies, planners, departments, and engineers to identify and prioritize locales where future site-specific liquefaction studies should be performed.

Anderson et al. (1982) previously developed a method to map liquefaction triggering potential for urban areas in twelve counties in Utah, including Utah County (Anderson et al., 1994a, b). To produce these maps, Anderson et al. computed the potential for liquefaction triggering at available SPT borehole and CPT sounding locations. They determined critical acceleration values needed to trigger liquefaction using a method introduced by Seed (1979). They then compared these critical accelerations to probabilistic predictions from seismic hazard analyses. Using surficial geologic maps as constraints, they generalized the results at each geotechnical investigation and produced qualitative liquefaction potential maps delineating zones of *low*, *moderate*, and *high* liquefaction potential. The Anderson et al. (1994a, b) hazard map of Utah County (see Fig. 2) shows high liquefaction potential for most of the urban area in the county. Although this map is a useful reference for liquefaction triggering, it is dated and does not estimate liquefaction effects such as lateral spread displacement.

To accomplish the 8 steps of the mapping method shown in Fig. 1 and summarized above, available data were compiled into a geospatial database, custom MATLAB scripts were written to perform the computations, and Esri's ArcMap® was used to visualize and analyze the outputs. This database is a portion of a larger geospatial database in state of Utah, GeoDU which has been compiled and used in other liquefaction mapping efforts (Gillins and Franke, 2016, Sharifi-Mood, 2017a, Gillins, 2012; Olsen et al., 2007; Erickson, 2006; Bartlett and Gillins, 2013). The following narrative provides details of each of the 8 steps of the mapping process, including the source of the data inputs and identification of any key assumptions. For additional details on the new Utah County liquefaction hazard maps, see Gillins and Franke (2016).

6.1. Step 1: input geology, slope, and free-face data

A vector-based geology base map of the study area (Constenius et al., 2011) was obtained from the Utah Geological Survey and input into a geospatial database. The Constenius et al. (2011) map is a compilation of detailed and recent mapping of several 7.5-min quadrangles at 1:24,000 to 1:50,000-scale along part of the populous Wasatch Front and Utah Valley. Fig. 3 presents the study area in Utah County and illustrates the surficial geologic units mapped by

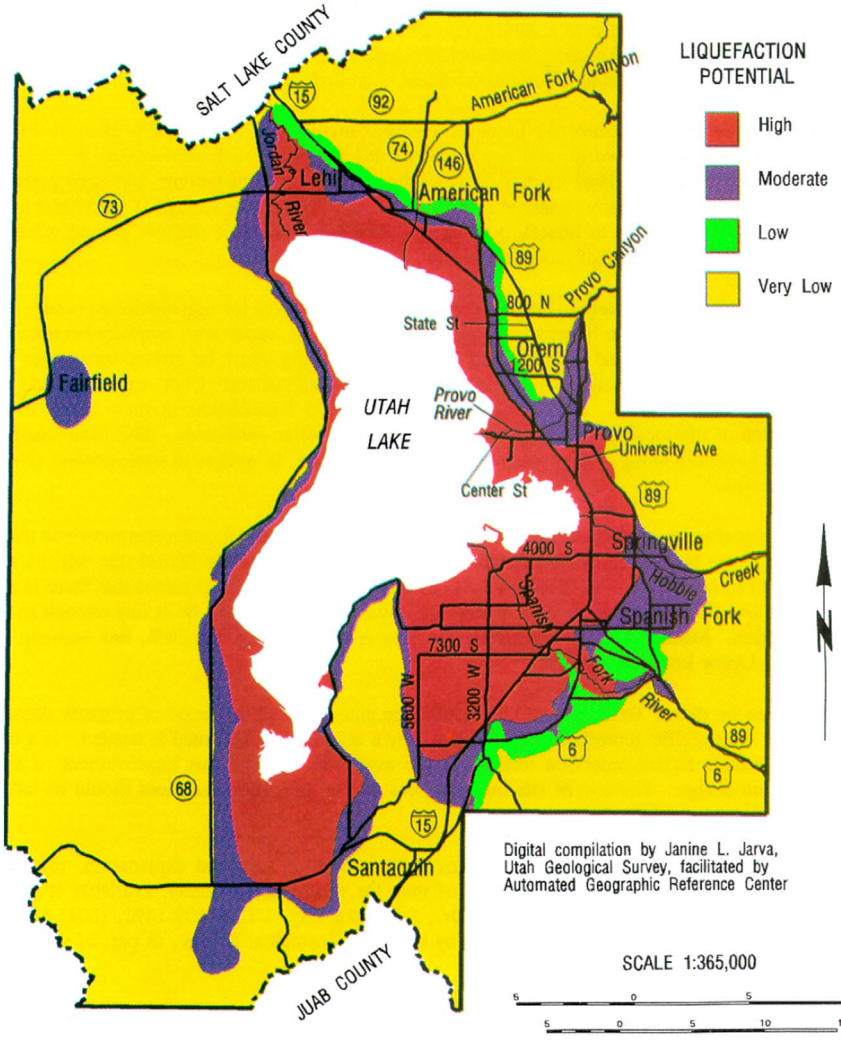

Fig. 2. Previous qualitative liquefaction potential hazard map developed by Anderson et al. (1994a, b) (reprinted with permission from the Utah Geological Survey).

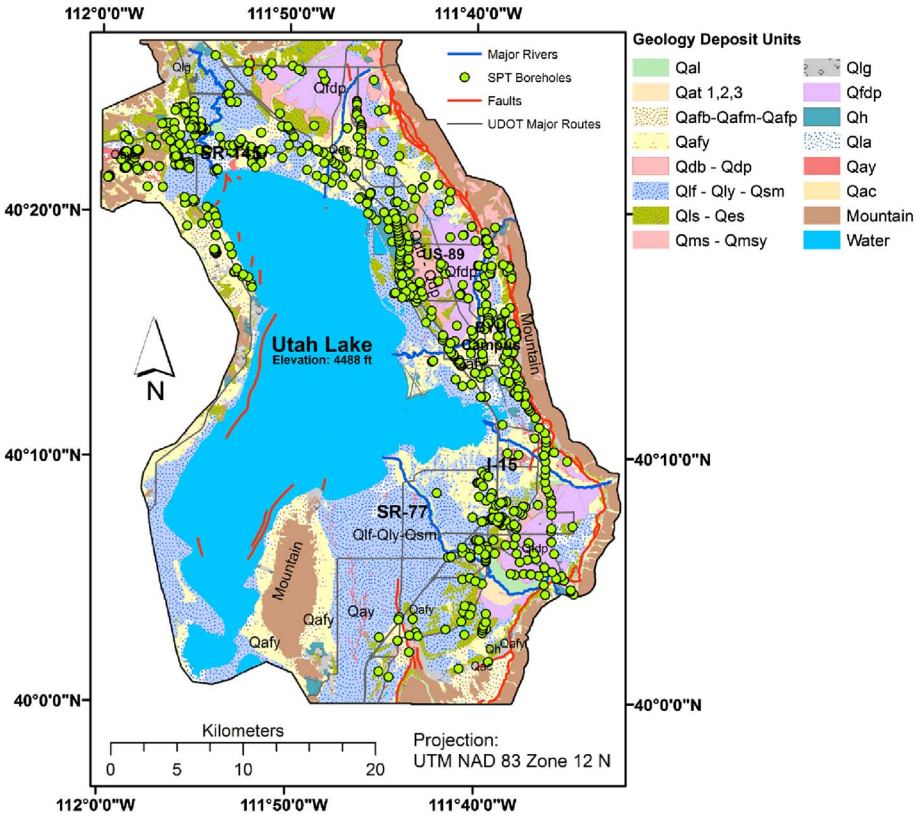

Fig. 3. Surficial geology and location of SPT boreholes in the study area, Utah County, Utah.

Constenius et al. (2011) with overlain locations of geotechnical explorations for the study, which will be discussed in Step 2 below. Holocene to Upper Pleistocene alluvial, lacustrine, and deltaic deposits are primarily shown on the map. Based on Youd and Perkins (1978), these deposits are moderately to very highly susceptible to liquefaction. The figure also depicts the Wasatch Mountains which bound the study area on the east, the Utah segment of the Wasatch Fault Zone (the primary seismic threat in Utah County), the extents of Utah Lake, and West Mountain to the south of Utah Lake. The study area is also bounded on the west by the Lake Mountains.

The authors grouped the quaternary geologic units in the study area into 14 categories, as tabulated in Table 3. Table 3 provides the symbol, description, and age for each of the units within the 14 categories from the Constenius et al. (2011) map. The geologic units depicted in Fig. 3 were then converted into a raster image, with values ranging from 1 to 14 corresponding to the definitions given in Table 3.

A 0.5-meter raster-based DEM of the study area was then downloaded from the Utah Automated Geographic Research Center (AGRC) (AGRC, 2014), and it was stored in the geospatial database. AGRC developed this DEM from aerial lidar data acquired in the fall of 2013 and the spring of 2014. The high-resolution DEM was useful for identifying slopes and free-faces in the study area. The ground slope (in percent) was computed, and the locations of the major free-faces in the study area were digitized. The Jordan and Provo River and some of their tributaries were considered as free-face features. Besides these river channels, areas that showed a dramatic change in elevation, which could be readily noticed when evaluating a hillshade of the DEM, were also digitized as free-face features.

During the digitization of the free-face features, a polyline feature class was drawn along the toe of that the identified free-face, and a polygon feature class was drawn to encompass areas above and affected by this free-face feature. The polyline and polygon feature were then converted to points at a spacing < 30 m. For each point within a polygon, multiple free-face ratios to all points along the toe were computed by dividing the difference in elevation with the horizontal distance from the site to the toe, and then the maximum free-face value was assigned as per a method in Gillins (2014). After repeating the process for all points and all free-face features in a custom MATLAB script, a natural neighbor interpolation among the points was used to output another raster that depicts the free-face ratio, W, for the study area.

The rasters of the surficial geology, slope, and free-faces were computed at a 30-m by 30-m pixel size. The lateral spread hazard was then evaluated for each individual pixel, resulting in final hazard maps.

6.2. Step 2: input geotechnical data and compute G

Available geotechnical investigations were collected, digitized, and stored in a geospatial database. Both SPT borehole logs and CPT soundings were acquired from multiple engineering firms and their clients, as well as government agencies such as the Utah Department of Transportation (UDOT), Utah Geological Survey (UGS), Central Utah Water Conservancy District (CUWCD), local city governments, and private entities. Overall, 753 borehole logs and 39 CPT soundings in the study area were collected, digitized, and stored in the database. Fig. 3 shows the spatial location of each SPT. As can be seen, numerous tests were found along the Interstate 15 corridor; however, some portions of the county with limited development (west and just southeast of Utah Lake) have sparser investigations.

Data from the SPT and CPT records were input into a database format that was developed and explained in Gillins (2012). Information such as soil descriptions and classifications, layer delineations, depths to groundwater, and uncorrected SPT blow counts (N_m) from the SPT logs were stored in the database. In addition, laboratory measurements on soil samples, such as fines contents, Atterberg limits, unit weights, and moisture contents were digitized. Friction ratio, sleeve friction, cone-tip resistance, and pore water pressure were stored from the CPT soundings. Most of the CPT soundings also had a pore-water pressure

Table 3
Geologic units in study area, descriptions, approximate age, and number of SPT logs.

Deposit symbol	Description	Age[a]	#SPT[b]
1. Stream alluvium			
Qal	Modern stream alluvium	H	20 (33)
2. Stream-terrace alluvium			
Qat_1	Stream-terrace alluvium, lowest terrace levels	H–UP	4 (7)
Qat_2	Stream-terrace alluvium, medium terrace levels	H–UP	2 (4)
Qat_3	Stream-terrace alluvium, highest terrace levels	H–UP	0 (1)
3. Alluvial fan – old			
Qafb	Transgressive (Bonneville) Lake Bonneville-age	UP	0 (1)
Qafm	Intermediate Lake Bonneville-age alluvial fan	UP to middle P	6 (21)
Qafp	Regressive (Provo) Lake Bonneville-age alluvial fan	UP	3 (10)
4. Alluvial fan – young			
Qafy	Younger alluvial-fan	H	98 (171)
5. Delta			
Qdb	Near Bonneville shoreline of Lake Bonneville	UP	1 (1)
Qdp	Near and below Provo shoreline of Lake Bonneville	UP	5 (13)
6. Fine-grained lacustrine			
Qlf	Fine-grained lacustrine from Lake Bonneville	UP	100 (194)
Qly	Young lacustrine < 6 m thick and overlies Qlf unit	H–UP	4 (6)
Qsm	Fine, organic-rich sediment from springs, marshes, seeps; < 3 m thick and overlies Qlf unit	H–UP	1 (1)
7. Lacustrine sand			
Qls	Lacustrine sand below Bonneville and Provo shorelines	UP	58 (100)
Qes	Eolian sand; 1–1.5 m thick and derived from Qls unit	H–UP	4 (7)
8. Landslides			
Qmsy	Modern landslide, currently or recently active	H	3 (6)
Qms	Modern landslide	H	2 (2)
9–14. Others			
Qlg	Lacustrine gravel and sand near Bonn. and Provo shorelines	Uppermost P	15 (21)
Qfdp	Lake Bonneville alluvial-fan and delta, Provo stage	Uppermost P	33 (61)
Qh	Human disturbance – fill for major interstate and highways	Historic	45 (53)
Qla	Lacustrine and alluvial, undivided	H–UP	14 (20)
Qay	Alluvial fan and terrace post-Provo shoreline of Lake Bonn.	H–UP	3 (13)
Qac	Alluvium and colluvium, undivided	Quaternary	3 (7)

[a] UP = Upper Pleistocene; P = Pleistocene; H = Holocene.
[b] Number in parenthesis is the grand total of SPTs in the unit. Number outside of parenthesis is the total of SPTs with maximum test depths > 7 m (20 ft) and that were actually used in the development of hazard map.

dissipation test data that gave an estimate of the depth to groundwater.

Table 3 shows the total number of SPT borehole logs in each of the 14 geologic categories in the study area. All 753 logs were used for characterizing the typical soil properties (e.g., moisture content, Atterberg limits, unit weights) for the geologic units; however, a large number of the tests (329) were quite shallow, and there was concern that some tests may not have encountered all of the soil layers at deeper depths which may liquefy and cause ground failures. Although all tests were used to characterize the geotechnical properties of the soil in Utah County, only SPTs that extended beyond a depth of 7 m were used when mapping the liquefaction hazard. Table 3 also provides a count of the number of SPT logs that reached a minimum depth of 7 m in all 14 geologic categories in the study area. A large number of SPT logs were available for the common units that cover the majority of the study area (e.g., Qafy, Qlf, Qfdp, Qls). Some of the units have a small number of SPT logs (e.g., Qms, Qat, Qd); however, one reason for this lack of sampling is because these units are rare in the study area. Future tests in under-developed portions of the study area, or in the geologic units with limited testing would undoubtedly improve the accuracy of the hazard maps. Future tests could be added to the Utah County geotechnical database, and new maps could then be produced that refine the maps presented in this paper.

A minimum termination depth of 7 m was chosen only as a compromise due to the limitations of the geotechnical database for Utah County. On one hand, overly shallow borehole tests may not have captured all of the layers of soil at a site that may liquefy during a major earthquake. On the other hand, if a deeper threshold was chosen, such as say 20 m, then over 300 of the SPT logs in the geotechnical database would have been screened out from the mapping process. In order to maintain as many available logs as possible for mapping the large study area while minimizing the use of overly shallow SPT logs, a threshold depth of 7 m was ultimately chosen.

During this step of the mapping process, a Monte Carlo simulation was initiated and a SPT borehole log was randomly selected from the total number of SPT logs that reached a minimum depth of 7 m in the geologic category for the selected pixel. For example, if the selected pixel was located in stream alluvium (i.e., Qal), then one of the 20 SPT boreholes collected in this geologic category was randomly selected. Then, $T_{15,\ cs}$ was computed for the selected borehole according to Eq. (3). Since each pixel was 30-m by 30-m, a semivariogram of $T_{15,\ cs}$ was not utilized for developing weights during the random selection of the SPTs in a geologic unit. The semivariogram reached a sill at just 30 m which is identical to the spatial resolution of the maps; therefore, even it was used, it would have affected at most $T_{15,\ cs}$ at four pixels per SPT.

To find $T_{15,\ cs}$ for a given borehole required several additional nested steps because only saturated soils that are susceptible to liquefaction should be considered. In general, moderate to high plasticity clays are not considered susceptible to liquefaction (Boulanger and Idriss, 2005; Bray and Sancio, 2006), although some have exhibited softening behavior that is somewhat similar to liquefiable soils during major earthquakes. Saturated, coarse-grained, cohesionless soils with low fines contents are widely considered susceptible to liquefaction. Clean sands are considered susceptible to liquefaction, and gravelly soils should be considered susceptible if they are bounded by materials with low permeability that allow build-up of excess pore-water pressure. It is much more difficult to define the susceptibility of soils with high fines contents (e.g., silty sands, clayey sands, sandy silts).

Boulanger and Idriss (2005) reviewed case histories and laboratory tests and identified two types of soil behavior on the basis of stress normalization and stress-strain response. Soils that exhibited *sand-like* behavior were considered susceptible to liquefaction, whereas soils that exhibited *clay-like* behavior were not considered susceptible. Boulanger

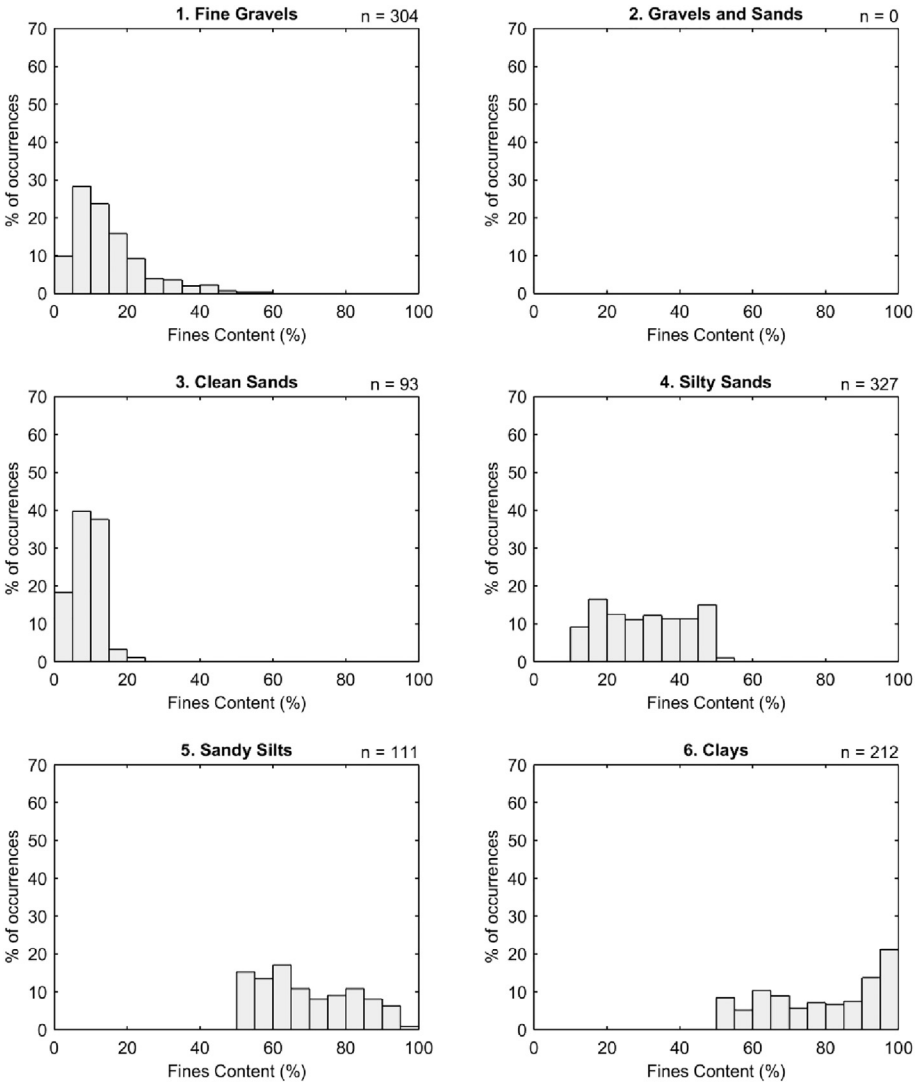

Fig. 4. Histograms for fines content for 6 different *SI* values, Utah County.

and Idriss found that soil plasticity can be used to determine if the soil will exhibit sand-like or clay-like behavior, and proposed that the soil is clearly sand-like at a plasticity index (PI) < 3, and a soil is clearly clay-like at a $PI > 8$. Although they noted a transitional phase between 3 and 8, ultimately they recommended that engineers use a conservative guideline with $PI = 7$ as the cutoff between sand-like and clay-like behavior when detailed laboratory testing is not possible. Thus, saturated soils with $PI < 7$ should be considered susceptible to liquefaction, and only layers of soil with these characteristics were considered when computing $T_{15,\ cs}$ at a selected borehole.

Unfortunately, values of *PI* as well as other soil properties were not reported for every layer of soil on the SPT logs in the geotechnical database. Thus, distributions of moisture contents, fines contents, and unit weights were developed using measurements recorded on *all* of the SPT logs in the database (i.e., including the shallow logs). As expected, the distributions for these properties varied by soil type. Thus, for every layer on each SPT log, an *SI* value was first assigned per Table 1. Fig. 4 shows one of the histograms of fines content, grouped according to *SI*. Refer to Gillins and Franke (2016) for other histograms of the dry unit weight, moisture content, and *PI* grouped by *SI* in Utah County. Nearly all of the soils with $SI = 6$ had a $PI > 7$, and almost all of the silts, sandy silts, and silty sands (i.e., $SI = 4$ or 5) had a $PI < 7$ in the database.

Following recommendations in Boulanger and Idriss (2005), the authors first only considered the saturated layers of soil in the SPT log with $PI < 7$ as susceptible to liquefaction when computing $T_{15,\ cs}$. However, some of the layers in the log lacked Atterberg limits, unit weights, moisture contents, and fines contents, all of which are necessary to correct raw SPT resistance (N_m) to $(N_1)_{60}$ to find $T_{15,\ cs}$. To rigorously account for this uncertainty and continue with the Monte Carlo simulation, values for moisture content, soil unit weight, and fines content were randomly sampled from the aforementioned distributions according to the *SI* of any layer in the log which lacked these data.

After simulating the missing data in the SPT log by random sampling for the i-th iteration of the Monte Carlo simulation, N_m was corrected to $(N_1)_{60}$ as:

$$(N_1)_{60} = C_E C_B C_R C_S C_N N_m \tag{12}$$

where C_E is the energy ratio correction factor accounting for the high variability in the amount of energy delivered to the drill rod stem by each impact of the SPT hammer, C_B is a correction factor for the borehole diameter, C_R is a correction factor for rod length, C_S is a correction factor for a sampler that had room for liners but was used without liners, and C_N is the overburden correction meant to account for the effects of increasing confining stress.

Recommended values and equations from Idriss and Boulanger (2008) were used for each of these SPT correction factors. Borehole

diameters, rod lengths, and the use of liners were reported on the SPT logs for computing C_B, C_R, and C_S, respectively. A value for C_N was computed for each simulation, because it is a function of the effective vertical stress and the soil stress profile varied slightly with each simulation according to the aforementioned randomly selected moisture contents and unit weights for those layers in the soil profile which lacked such data.

Many of the logs only reported the hammer release type (i.e., automatic or safety hammer) and did not include measurements of the energy delivered to the hammer for estimating C_E. Idriss and Boulanger (2008) report ranges of possible values for C_E according to the hammer type. For a safety hammer, C_E is reported to range from 0.7 to 1.2; for an automatic hammer, the range for C_E is reported as 0.8 to 1.3. (Note that none of the logs in the geotechnical database involved the use of a doughnut hammer.) It was assumed that these possible ranges for C_E are normally distributed, with a mean equal to the middle of the range, and a standard deviation equal to one-sixth of the range. Thus, for the i-th simulation, a value for C_E was estimated ($C_{E,\,i}$) as:

$$C_{E,i} = \overline{C_E} + \sigma_{C_E}.\, K_{rand,i} \tag{13}$$

where $\overline{C_E}$ is a value of 1.0 or 1.1 for the safety hammer or automatic hammer, respectively, σ_{C_E} is a equal to 0.08 for both hammers, and $K_{rand,\,i}$ is a random number generated for the simulation that follows the standard normal distribution.

After correcting (N_m) to $(N_1)_{60}$ for the i-th simulation, $T_{15,\,cs,\,i}$ for the i-th simulation was next found by computing the thickness of only those saturated layers of soil with a value of $(N_1)_{60} < 15$ and with either: (1) a measured $PI < 7$, or (2) a value of $SI \leq 5$ if the PI for the layer was not recorded on the log.

The computed values for $T_{15,\,cs,\,i}$, W, and S (from the Step 1) were used with Eq. (5) to compute G_i. The regression coefficients for Eq. (5) vary depending on the topography at the point of interest. For conservatism, Eq. (5) was therefore solved twice—once for free-face conditions and once for ground-slope conditions. Then, the smaller of the two resulting values of G (i.e., the one that would produce the larger predicted lateral spread displacement) was assigned as G_i for the simulation.

6.3. Step 3: input seismic loading

Continuing with the i-th simulation, the next step was to randomly select and input an apparent loading value, $\mathscr{L}_i$, from the PDF of $\mathscr{L}$ at the selected pixel. To develop the PDF, EZ-FRISK, 2015 software (version 7.62) was used to output hazard curves for $\mathscr{L}$ from a PSHA at grid points evenly spaced every 0.05 degrees in latitude and longitude (roughly every 3 to 5 km) across the study area. Franke (2005) outlined a procedure for programming EZ-FRISK, 2015 to output an $\mathscr{L}$-hazard curve using its *Attenuation Table* feature. To use this table, values of $\mathscr{L}$ were entered by solving Eq. (4) at incremented values of M from 4.6 to 8.4 (based on the normal crustal faults in Utah County, in increments of 0.2), and values of R of 1, 5, 10, 15, 20, 25, 30, 40, 50, 60, 70, 80, 90, 100, 125, 150, 175, 200, 250, and 300 km. EZ-FRISK, 2015 was set to use the USGS 2008 faults, areas, and background sources to perform the PSHAs (Petersen et al., 2008). The 2014 USGS models were not available in EZ-FRISK, 2015 at the time of the study. All USGS seismic sources within 500 km of each grid point were included in the PSHAs, and hazard values for $\mathscr{L}$ were output for return periods of 100, 275, 475, 1000, 2500, 5000, and 10,000 years. Fig. 5 presents $\mathscr{L}$ -hazard curves at four grid points in the study area. The location of these four grid points is shown in Fig. 6. Seven 30-m resolution raster images of $\mathscr{L}$ for the above return periods were generated by bilinear interpolation of the $\mathscr{L}$-hazard curves computed at the evenly spaced grid points. Fig. 6 illustrates three of these raster images for $\mathscr{L}$ at return periods of 1000, 2500, and 5000 years.

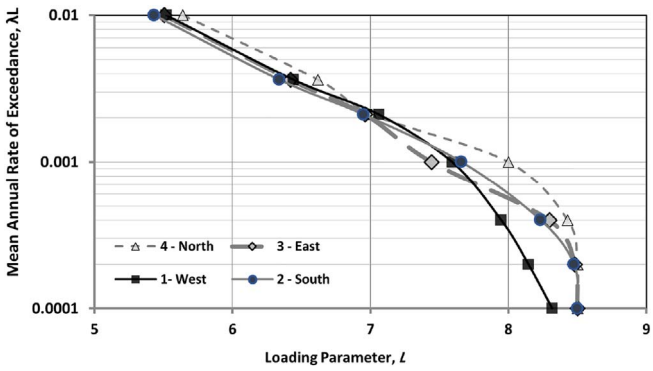

Fig. 5. Apparent loading parameter hazard curves for four discrete locations in Utah County; which are identified in Fig. 6.

To perform the third step of the mapping process and continue with the i-th simulation, values for $\mathscr{L}$ were first extracted from each of the seven rasters at the selected pixel. This produced seven intermediate points on an $\mathscr{L}$ -hazard curve at the pixel (similar to the points on the curves depicted in Fig. 5). The points were then converted to units of return period so that an eighth intermediate point at (0,0) could be added. A linear interpolation (in increments of 0.1) between each of the eight intermediate points was then applied to the logarithm of the return period of the points, enabling production of numerous points along the $\mathscr{L}$-hazard curve at the mapping pixel. The exceedance probability for each of the points on the hazard curve was then computed using a Poisson probability distribution, and the results were binned into a PDF for binned values of $\mathscr{L}$. Next, a value for $\mathscr{L}_i$ was randomly selected from the PDF for $\mathscr{L}$ at the pixel.

6.4. Step 4: compute $logD_H$

Continuing with the i-th simulation, G_i from Step 2 and $\mathscr{L}_i$ from Step 3 were summed to find $\overline{log\,D_{H\,i}}$, then error in the lateral spread displacement model was simulated by solving Eq. (10) in order to output a value for $[logD_H]_i$.

6.5. Step 5: repeat steps 2–4, produce D_H distribution

Numerous simulations are necessary to model the several sources of uncertainty in the subsurface characterization (i.e., $(N_1)_{60}$, $T_{15,\,cs}$, C_E), seismic hazard (i.e., $\mathscr{L}$), and lateral spread displacement modeling error (i.e., ε). As further discussed below, Steps 2–4 were repeated 200,000 times for each pixel, resulting in a distribution of $logD_H$ values at each pixel. This distribution was then converted into a distribution of D_H values (in meters). Note a new SPT for a given geologic unit was randomly selected for each simulation with replacement.

6.6. Step 6: compute D_H hazard curve

The next step in the mapping procedure was to convert the 200,000 D_H values at a pixel from the Monte Carlo simulations into a D_H-hazard curve. To make this conversion, the distribution for D_H was first converted into an empirical cumulative distribution function (CDF) curve. The annual probability that D_H exceeds a displacement value, d, of interest (i.e., $P(D_H > d)$) is equal to *1 minus the CDF* value at d on this curve. (Note that the CDF is always equal to the non-exceedance probability; therefore, in this case, the CDF equals the probability D_H does not exceed d). The annual exceedance probability was defined using the Poisson model (Eq. (11)), where $t = 1$ year for an annual probability, and λ = the mean annual rate of exceedance.

Table 4 lists some typical return periods of interest and their corresponding values of λ, annual exceedance probability, and CDF. Using the empirical CDF, points on the D_H-hazard curve at a selected pixel

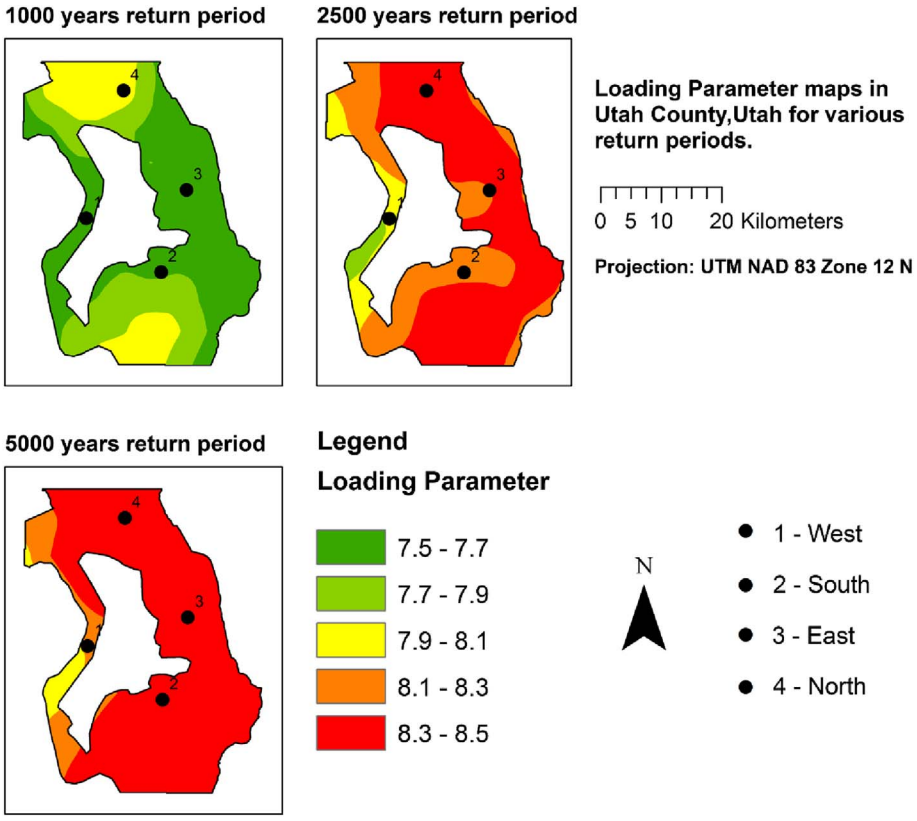

Fig. 6. Apparent loading parameter hazard maps for a 1000-year, 2500-year, and 5000-year return period in Utah County.

Table 4
Example distribution of D_H values at listed return periods.

Return period [1/λ] (years)	Mean annual rate of exceedance, λ	Annual exceedance probability [$P(D_H > d)$]	CDF [$P(D_H < d)$]	d (meters)
108	0.01	0.009	0.991	0.00
228	0.004	0.0044	0.9956	0.00
475	0.002	0.0021	0.9979	0.01
1033	0.001	0.0010	0.9990	0.06
2475	0.0004	0.00040	0.99960	0.43
4975	0.0002	0.00020	0.99980	1.84
9975	0.0001	0.00010	0.99990	3.45

were developed by finding the displacement value at each of the CDF values listed in Table 4. As an example, the fifth column of Table 4 presents a set of displacement values taken from an empirical CDF at a particular pixel in the study area. Plotting λ versus d from Table 4, the D_H-hazard curve for this example set of data can be depicted, as shown in Fig. 7a.

It is interesting to consider the meaning of the hazard curve depicted in Fig. 7a and tabulated in Table 4. For a 475-year or 2475-year return period hazard, the annual exceedance probability equals only 0.2% and 0.04%, respectively. Clearly, for a given year, these extreme hazard levels are highly unlikely; nonetheless, engineers are concerned with such hazard levels because the extreme events can cause significant damage. Upon further inspection of the example data in Table 4, 0.2% (or 400 of the 200,000 simulations) of the data in the D_H distribution at the mapping pixel exceeded a displacement value of 0.01 m, and only 0.04% (or 80 of the 200,000 simulations) exceeded a displacement value of 0.43 m. These lateral spread displacement values of 0.01 m and 0.43 m therefore correspond to the 475-year and 2475-year return period hazards, respectively.

Since the extreme values in the D_H distributions are of greatest interest when mapping the lateral spread hazard, it is important to perform many Monte Carlo simulations. In addition, numerous simulations ensure that the uncertainties in the mapping process are modeled well. The authors decided to run 200,000 simulations for each pixel. This large number was selected because it produced a D_H-hazard curve that looked similar to a D_H-hazard curve after 300,000 or 400,000 simulations at return periods $<$ 2475 years, and it did not overburden the computer with excessive computational time. For example, Fig. 7b presents D_H-hazard curves at the same mapping pixel after running 10,000, 50,000, 100,000, 200,000, 300,000, and 400,000 simulations. The curve for 10,000 simulations appears different than the other curves, and the authors concluded after several tests at numerous pixels that this number of simulations was inadequate. The curves appear fairly similar when $N \geq$ 100,000 simulations, especially at return periods $<$ 2475 years (i.e., $\lambda < 0.0004$).

6.7. Step 7: repeat steps 1–6 for all map pixels

The first six steps of the mapping procedure were repeated for every pixel in the study area. Upon completion, a D_H-hazard curve similar to the one depicted in Fig. 7a was generated for every pixel.

6.8. Step 8: output D_H hazard map

The final step was to produce 30-m resolution raster hazard maps at the desired return periods. This was performed by simply extracting the D_H value from the D_H -hazard curve at a desired return period (e.g., 475, 1,33, or 2475-year return period) for each pixel, and then storing the extracted data as raster values in a raster image of the study area. Because the D_H -hazard curves were already computed at a resolution of 30-m for the study area, no additional interpolation was necessary. The raster images for return periods of 1033, and 2475 years were visualized in GIS to produce the final hazard maps (Figs. 8 and 9).

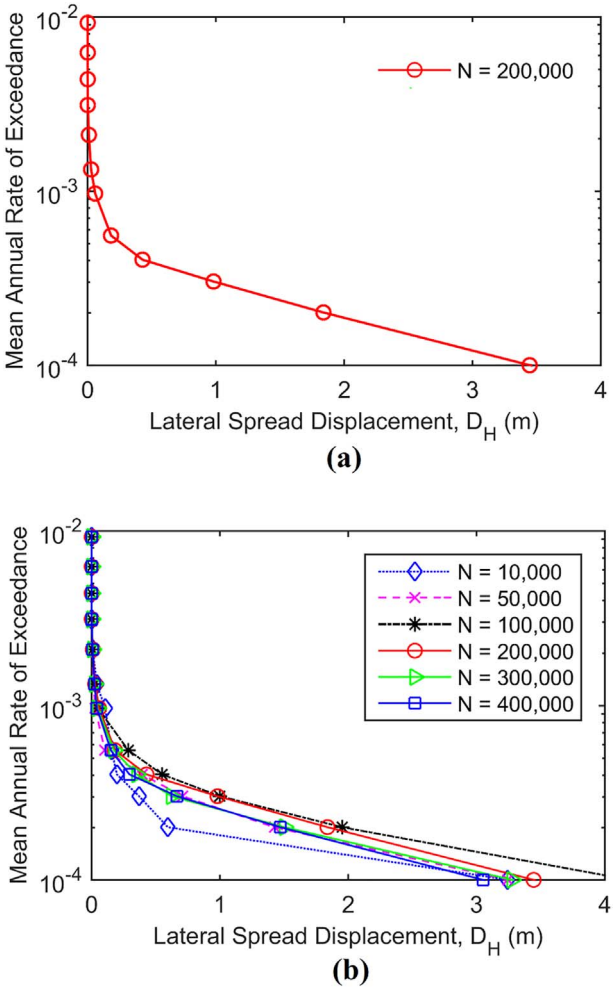

Fig. 7. (a) Example D_H-hazard curve at a mapping pixel after 200,000 Monte Carlo simulations; (b) a set of D_H -hazard curves at the same mapping pixel after different numbers of Monte Carlo simulations.

7. Results and discussion

The Anderson et al. (1994a, b) map (Fig. 2) indicates that a significant portion of the study area has *high* liquefaction potential. However, this map does not give any indication of the severity of ground failures nor does it show possible consequences like lateral spread. Mapping lateral spread displacements such as those in Figs. 8 and 9 is advantageous because large displacements are strongly correlated with potential damage.

Fig. 8 shows that lateral spread displacements are not generally expected to exceed 0.1 m for almost the entire study area at a return period of 1033 years. Nevertheless, the map does show some displacements may reach up to 0.3 m in some of the lacustrine sand and young alluvial fan units with sufficient topographic relief (i.e., near a free-face or on sloping ground). Except for these relatively small locales, it is concluded that the lateral spread hazard is minimal at the 1033-year return period in most of the study area. This finding highlights one of the benefits of producing fully-probabilistic hazard maps. Some building codes require design engineers to evaluate structures, foundations, and lifelines to withstand a 475-year or 1033-year return period hazard. Our results at this return period indicate that the potential for significant lateral spread displacement and damage are very localized.

However, for critical infrastructure, building codes may require engineers to evaluate the hazard for less frequent events (i.e., lower probability of non-exceedance) (Olsen et al., 2015). Based on our mapping efforts, we conclude that some locations in the study area may experience significant lateral spread displacements at the 2475-year return period hazard level. Fig. 9 shows limited portions of the study area that may undergo displacements $>$ 1 m and some areas may experience displacements exceeding 0.3 m. In short locales having the combined characteristics of liquefiable layers with sufficient $T_{15,\ cs}$ values, topographic relief, and apparent seismic loading may undergo damaging horizontal displacement during major, nearby earthquakes. Notwithstanding, even though the map does suggest the potential for significant lateral spread hazard in localized areas, the majority of the map generally shows displacements $<$ 0.3 m.

In additional evaluations, it was found that when simulating a major earthquake (i.e., large value for $\mathscr{L}$) as a result of fault rupture of the nearby Utah segment of the Wasatch Fault Zone, the relatively high estimated strong motion and its close proximity to the study area frequently produced at least small D_H values ranging from 0.1 to 0.3 m in geologic units with nonzero $T_{15,\ cs}$values.

Fig. 10 presents D_H-hazard curves at 4 points of interest, as located in Figs. 8 and 9. The Figure highlights how the displacement hazard varies in the study area. For example, Point III is near the I-15 corridor, north of Utah Lake. The lateral spread displacement hazard was greatest at this point as compared with the other points. Point I is west of Utah Lake and has the lowest displacement hazard as compared with the other points. This is likely because Point I has a lower apparent loading hazard as it is further from the Wasatch Fault Zone.

It is worth noting that the geologic map for Utah County (Fig. 3) identifies some small deposits east of the I-15 corridor and southeasterly of Utah Lake which may have underwent lateral spreading during a prehistoric earthquake. These deposits were labeled as "*Qml? Lateral-spread deposits?*" on the Constenius et al. (2011) map. Unfortunately, none of the available investigations in the geotechnical database were within these deposits. Given that they may have underwent lateral spreading in the past, and because of a lack of geotechnical data in these deposits, these areas were hatched in hazard maps in Figs. 8 and 9. Further research is needed to determine the lateral spread hazard for the *Qml?* unit.

8. Conclusions

This paper proposed methods to develop fully probabilistic lateral spread displacement hazard maps using available seismic, geotechnical, geological and topographical data. These methods were then implemented to produce hazard maps at return periods of 1033 and 2475 years for Utah County, Utah. Although the paper focused on this county, other areas could also be mapped following similar procedures.

The lateral spread displacement map show a negligible displacement hazard at a return period of 1033 years. However, at the more extreme 2475-year return period, estimated displacements may exceed 1 m in a few locations in the study area. This is because: (1) numerous SPT borehole logs in the geotechnical database show layers of loosely deposited, cohesionless soils; (2) a significant portion of the area has a shallow groundwater table due to its proximity to Utah Lake; and (3) the area is in very close proximity to the Utah segment of the Wasatch Fault Zone which is capable of generating a major earthquake with $M_w \geq 7$. Clearly, liquefaction and its effects should be a major concern for Utah County as well as other parts of the Wasatch Front. It is recommended to conduct additional site-specific studies at areas with high lateral spread hazard.

The methods presented in this paper are new and innovative. First, the hazard maps are based on seismic loading from a fully probabilistic seismic hazard analysis (PSHA). Previous liquefaction hazard mapping efforts (e.g., Anderson et al., 1982; Bartlett et al., 2005; Baise et al., 2006; Holzer et al., 2006; Olsen et al., 2007; Gillins, 2012) show hazard levels given either a constant peak ground acceleration for the entire study area, a deterministic scenario event, or an event from a single return period of the deaggregation of a probabilistic seismic hazard

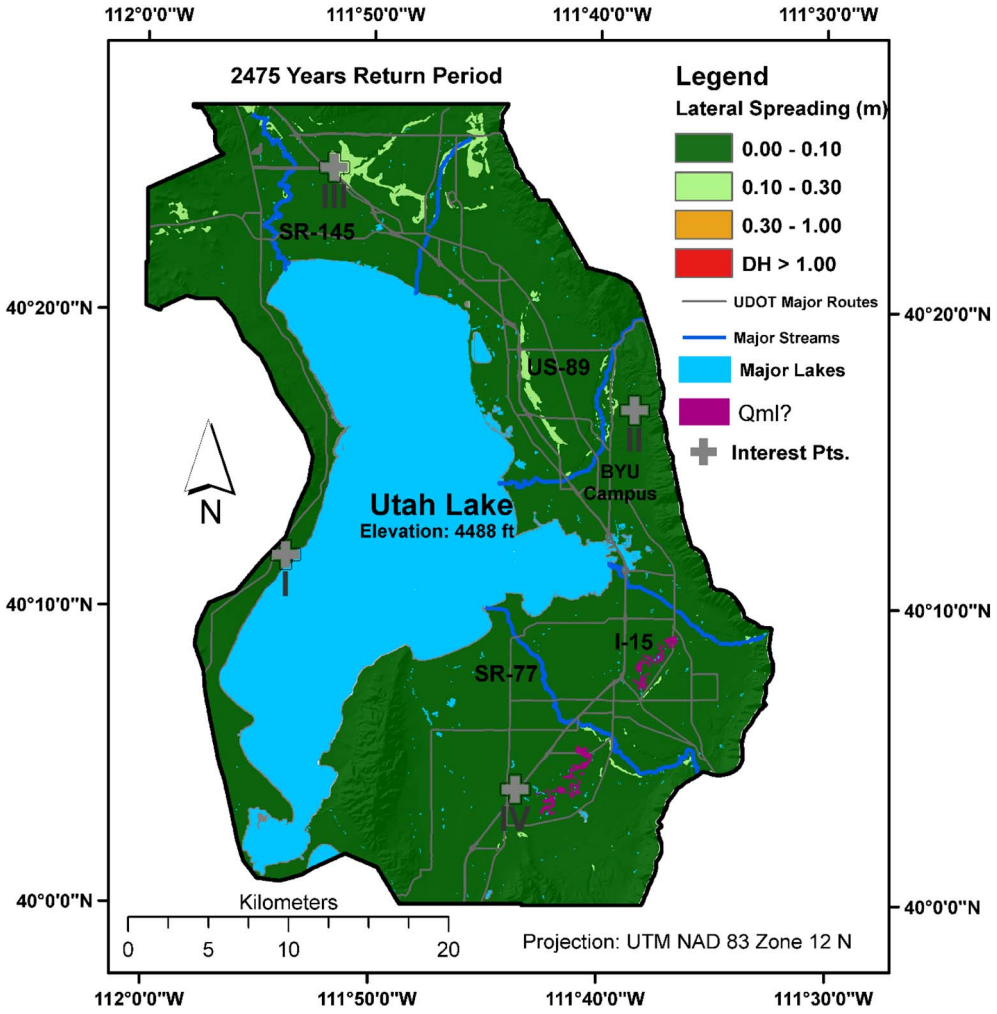

Fig. 8. The 1033-year return period lateral spread hazard map, Utah County, Utah.

analysis. Second, using Monte Carlo random sampling techniques, the maps presented in this paper modeled the uncertainty in the in state-of-the-art lateral spread displacement (i.e., Gillins and Bartlett, 2013) empirical equation by using its published standard deviation per Eq. (10). Lastly, the lateral spread hazard maps modeled the spatial variation in ground slopes and free faces using a highly-resolute DEM developed from aerial lidar data collected in 2013.

The maps are intended to convey preliminary hazard information to city planners, developers, and engineers. Because mapping liquefaction and ground displacement hazards for a regional area is challenging, the authors recognize some parts of the maps have large uncertainty, and perhaps errors associated with the data. Although the maps are based on over 750 geotechnical boreholes, significant uncertainties remain in the subsurface conditions. For example, the authors noticed marked variability in the results of SPT investigations—even for those found in the same geologic unit and located within 100 m of each other. The authors attempted to account for this variability while mapping Utah County by developing distributions of geotechnical properties using tens to hundreds of available SPT boreholes found in each geologic unit. However, it is inappropriate to assume that a few local SPT investigations at a discrete location fully characterizes the uncertainties in subsurface conditions for an entire, widespread geologic unit. Therefore, it is hoped that practicing professionals will continue performing site-specific evaluations, especially in areas mapped with high lateral spread displacement hazard in order to refine the mapped estimates. Furthermore, by conducting and compiling additional investigations, it would be possible to update and improve the maps as the dataset and knowledge evolve. For example, the maps could be updated when new earthquake models or strong motion estimates are published by the USGS, or as new or revised lateral spread displacement models become available.

Although the mapping methodology discussed herein should be considered a step forward from previous hazard mapping efforts, the presented maps are still not intended nor recommended for site-specific engineering evaluations and design. The authors strongly encourage individuals engaged in evaluating, designing, building, or maintaining infrastructure—especially critical infrastructure—to continue performing site-specific liquefaction hazard evaluations using qualified experts. Experienced professionals should be consulted regarding their knowledge of the study area based on prior geologic mapping and geotechnical investigative efforts. Such experts may be able to note discrete areas on the hazard maps that are inconsistent with their knowledge and experience of the conditions at specific locales.

More site-specific testing will be invaluable and the new geotechnical investigations could be added to the geotechnical database in order to improve the characterization of the subsurface. The maps presented herein for Utah County are based on available SPTs collected in a non-systematic manner over multiple decades. A higher density of geotechnical investigations distributed more thoroughly across the study area could be used to improve the accuracy of the maps presented in this paper. With more SPTs, it may be possible to spatially interpolate $T_{15,cs}$ through the SPT locations using some type of geostatistical method, such as has been done for other study areas (e.g., Liu et al., 2016; Juang et al., 2017; Baker and Faber, 2008; Chen et al., 2016),

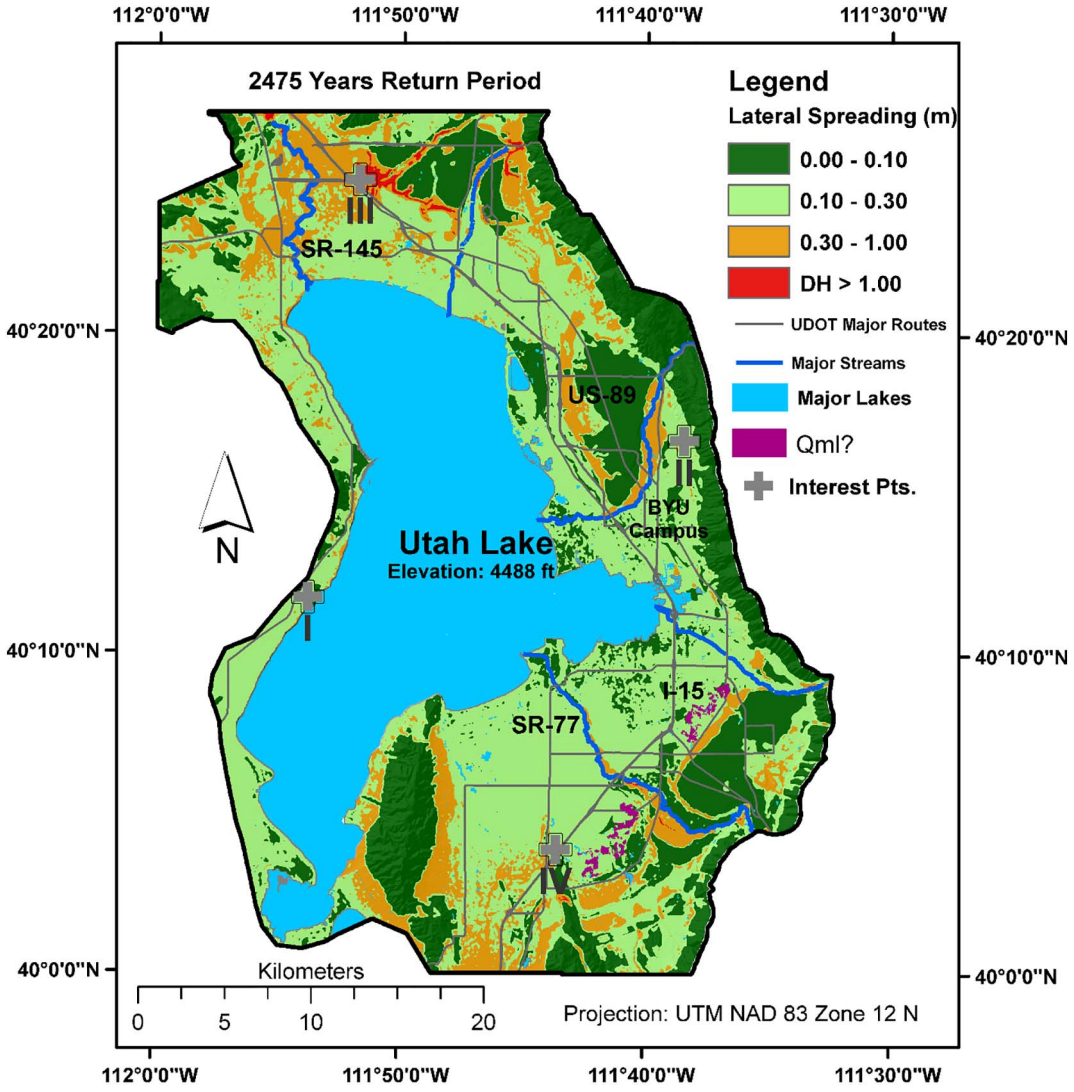

Fig. 9. The 2475-year return period lateral spread displacement hazard map, Utah County, Utah.

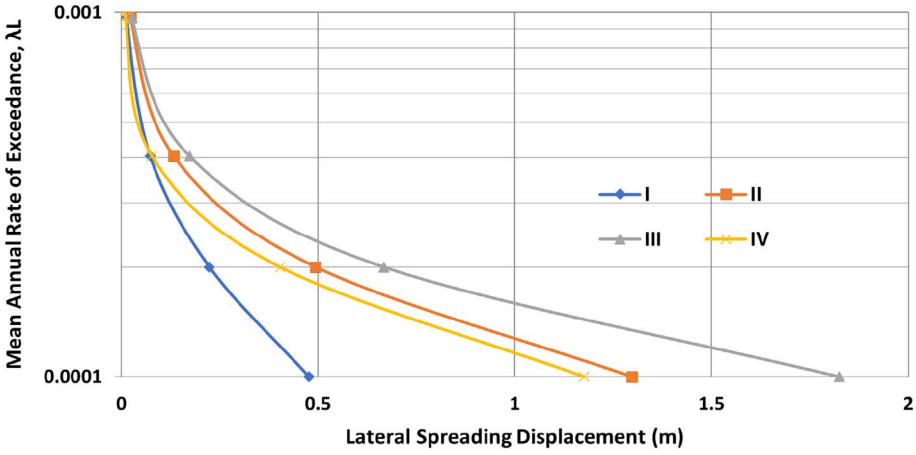

Fig. 10. Lateral spreading displacement hazard curves for 4 points of interest in the study area.

than estimating $T_{15,cs}$ from sets of SPTs for each geologic unit. Moreover, it could allow development of a realistic ground water table model and possibly a reliable 3D subsurface model for future hazard mapping.

Acknowledgements

This research was supported by the U.S. Geological Survey (USGS), Department of the Interior, under USGS award numbers G14AP00118 and G14AP00119, as well as by the Utah Department of Transportation

and the Central Utah and Weber Basin Water Conservancy Districts. The views and conclusions contained in this document are those of the authors and should not be interpreted as necessarily representing the official policies, either expressed or implied, of these government agencies.

References

Anderson, L.R., Keaton, J.R., Aubrey, Kevin, Ellis, S.J., 1982. "Liquefaction Potential Map for Davis County, Utah," Logan, Utah State University Department of Civil and Environmental Engineering and Dames and Moore unpublished Final Technical Report prepared for the U.S. Geological Survey, National Earthquake Hazards Reduction Program Award No. 14-08-0001-19127, 50 p.; Published as Utah Geological Survey Contract Report 94-7, 1994.

Anderson, L.R., Keaton, J.R., Bischoff, J.E., 1994a. "Liquefaction Potential Map for Utah County, Utah," Logan, Utah State University Department of Civil and Environmental Engineering and Dames and Moore unpublished Final Technical Report prepared for the U.S. Geological Survey, National Earthquake Hazards Reduction Program Award No. 14-08-0001-21359, 46 p., 1986; Published as Utah Geological Survey Contract Report 94-8, 1994.

Anderson, L.R., Keaton, J.R., Eldredge, S.N., 1994b. Liquefaction-potential Map for a Part of Utah County, Utah: Utah Geological Survey Public Information Series 28, 2 p., scale 1:365,000 (at). http://ugspub.nr.utah.gov/publications/public_information/pi-28.pdf, Accessed date: 6 June 2017.

Automated Geographic Reference Center (AGRC), 2014. Wasatch front lidar, state of Utah (acquired from). http://gis.utah.gov/data/elevation-terrain-data/2013-2014-lidar/.

Baise, L.G., Higgins, R.B., Brankman, C.M., 2006. Liquefaction hazard mapping – statistical and spatial characterization of susceptible units. J. Geotech. Geoenviron. Eng. 132 (6), 705–715.

Baker, J.W., Faber, M.H., 2008. Liquefaction risk assessment using geostatistics to account for soil spatial variability. J. Geotech. Geoenviron. 134 (1), 14–23.

Bartlett, S.F, Gillins, D.T., 2013. Mapping the probability and uncertainty of liquefaction-induced ground failure for Weber County, Utah. USGS External Research Award. (G12AP20074).

Bardet, J.P., Tobita, T., Mace, N., Hu, J., 2002. Regional modeling of liquefaction-induced ground deformation. Earthquake Spectra 18 (1), 19–46.

Bartlett, S.F., Youd, T.L., 1995. Empirical prediction of liquefaction-induced lateral spread. J. Geotech. Eng. 121 (4), 316–329.

Bartlett, S.F., Olsen, M.J., Solomon, B.J., 2005. "Lateral Spread Hazard Mapping of Northern Salt Lake County for a Magnitude 7.0 Scenario Earthquake," Technical Report Submitted to the United States Geological Survey, NERHP Award No. 04HQGR0026. (218 pp.).

Bazzurro, P., Cornell, C.A., 2004. Nonlinear soil-site effects in probabilistic seismic-hazard analysis. Bull. Seismol. Soc. Am. 94 (6), 2110–2123.

Boulanger, R.W., Idriss, I.M., 2005. "Evaluating Cyclic Failure in Silts and Clays," Proc. of Geotechnical Earthquake Engrg. Satellite Conf. on Performance-Based Design in Earthquake Geotech. Engrg: Concepts and Research. Prepared by TC4 Committee of ICSMGE, Japanese Geotechnical Society, Tokyo. pp. 78–86.

Bray, J.D., Sancio, R.B., 2006. Assessment of the liquefaction susceptibility of fine-grained soils. J. Geotech. Geoenviron. Eng. 132 (9), 1165–1177.

Bray, J.D., Travasarou, T., 2007. Simplified procedure for estimating earthquake-induced deviatoric slope displacements. J. Geotech. Geoenviron. Eng. 133 (4), 381–392.

Chen, Q., Wang, C., Juang, C.H., 2016. Probabilistic and spatial assessment of liquefaction-induced settlements through multiscale random field models. Eng. Geol. 211, 135–149.

Constenius, K.N., Clark, D.L., King, J.K., Buck Ehler, J., 2011. "Interim Geologic Map of the Provo 30′ × 60′ Quadrangle, Utah, Wasatch, and Salt Lake Counties, Utah," Open-File Report 586DM, Utah Geological Survey.

Cornell, C.A., Krawinkler, H., 2000. Progress and challenges in seismic performance assessment. PEER Cent. News 3 (2), 1–4.

Cramer, C.H., Rix, G.J., Tucker, K., 2008. Probabilistic liquefaction hazard maps for Memphis, Tennessee. Seismol. Res. Lett. 79 (3), 416–423.

Deierlein, G.G., Krawinkler, H., Cornell, C.A., 2003. A framework for performance-based earthquake engineering. In: Proc., 2003 Pacific Conf. on Earthquake Engineering.

Erickson, G.L., 2006. Probabilistic liquefaction potential mapping of the Salt Lake Valley. M.S Thesis. Univ. of Utah, Salt Lake City.

EZ-FRISK, 2015. Software for Earthquake Ground Motion Estimation.

Faris, A.T., Seed, R.B., Kayen, R.E., Wu, J., 2006. A semi-empirical model for the estimation of maximum horizontal displacement due to liquefaction-induced lateral spreading. In: Proc., 8th U.S. Nat. Conf. Earthquake Engrg Vol. 3. Earthquake Engineering Research Institute, Oakland, CA, pp. 1583–1584.

Franke, K.W., 2005. Development of a Performance-Based Model for the Prediction of Lateral Spreading Displacements (M.S. thesis). Univ. of Washington, Seattle.

Franke, K.W., Kramer, S.L., 2014. Procedure for the empirical evaluation of lateral spread displacement hazard curves. J. Geotech. Geoenviron. Eng. 140 (1), 110–120.

Gillins, D.T., 2012. Mapping the Probability and Uncertainty of Liquefaction-Induced Ground Failure (Ph.D. Dissertation). Univ. of Utah, Salt Lake City.

Gillins, D.T., 2014. Considering topography when mapping liquefaction hazard with the liquefaction potential index. In: Proc. 10th National Conf. on Earthquake Engrg., Anchorage, Alaska, (July 21–25, 12 pp.).

Gillins, D.T., Bartlett, S.F., 2013. Multilinear regression equations for predicting lateral spread displacement from soil type and cone penetration test data. J. Geotech. Geoenviron. Eng. 140 (4), 04013047.

Gillins, D.T., Franke, K., 2016. "Probabilistic Liquefaction Potential and Lateral Spread Hazard Maps for Utah County, Utah: Collaborative Research with Brigham Young University and Oregon State University", USGS External Research Report, USGS Award Nos. G14AP00118 and G14AP00119, Reston, VA. (89 pp.).

Hamada, M., Yasuda, S., Isoyama, R., Emoto, K., 1986. Study on liquefaction induced permanent ground displacements. In: Report for the Association for the Development of Earthquake Prediction in Japan, Tokyo, Japan, (87 pp.).

Holzer, T.L., Blair, J.L., Noce, T.E., Bennett, M.J., 2006. LiqueMap: a real-time post earthquake map of liquefaction probability. In: Proc., 8th US National Conference on Earthquake Eng., EERI, Oakland, CA.

Idriss, I.M., Boulanger, R.W., 2008. Soil liquefaction during earthquakes. In: Earthquake Engineering Research Institute Monograph MNO-12. Earthquake Engineering Research Institute, Oakland, CA (262 pp.).

Iwasaki, T., Tokida, K., Tatsuoka, F., Watanabe, S., Yasuda, S., Sato, H., 1982. Microzonation for soil liquefaction potential using simplified methods. In: Proceedings of the 3rd International Conference on Microzonation, Seattle Vol. 3. pp. 1310–1330.

Jaimes, M.A., Niño, M., Reinoso, E., 2015. Regional map of earthquake-induced liquefaction hazard using the lateral spreading displacement index D LL. Nat. Hazards 77 (3), 1595–1618.

Juang, C.H., Shen, M., Wang, C., et al., 2017. Random field-based regional liquefaction hazard mapping—data inference and model verification using a synthetic digital soil field. Bull. Eng. Geol. Environ. http://dx.doi.org/10.1007/s10064-017-1071-y.

Lam, I., Arduino, P., Mackenzie-Helnwein, P., 2009. OpenSees soilpile interation study under lateral spread loading. In: Int. Foundation Congress & Equipment Expo '09. ASCE, Reston, VA, pp. 206–213.

Lee, D.H., Ku, C.S., Yuan, H., 2004. A study of the liquefaction risk potential at Yuanlin, Taiwan. Eng. Geol. 71 (1), 97–117.

Lenz, J.A., Baise, L.G., 2007. Spatial variability of liquefaction potential in regional mapping using CPT and SPT data. Soil Dyn. Earthq. Eng. 27 (7), 690–702.

Liu, F., Li, Z., Jiang, M., Frattini, P., Crosta, G., 2016. Quantitative liquefaction-induced lateral spread hazard mapping. Eng. Geol. 207, 36–47.

Luna, R., Frost, J.D., 1998. Spatial liquefaction analysis system. J. Comput. Civ. Eng. 12 (1), 48–56.

Mabey, M.A., Madin, I., 1993. Relative Earthquake Hazard Map: Portland, Oregon 7–1/2 Minute Quadrangle. Oregon Department of Geology and Mineral Industries.

Maurer, B.W., Green, R.A., Cubrinovski, M., Bradley, B.A., 2014. Evaluation of the liquefaction potential index for assessing liquefaction hazard in Christchurch, New Zealand. J. Geotech. Geoenviron. 140 (7), 04014032.

Olsen, M.J., Ashford, S.A., Mahlingam, R., Sharifi-Mood, M., O'Banion, M., Gillins, D.T., 2015. Impacts of Potential Seismic Landslides on Lifeline Corridors. (No. FHWA-OR-RD-15-06).

Olsen, M.J., Bartlett, S.F., Solomon, B.J., 2007. Lateral spread hazard mapping of the northern salt Lake Valley, Utah, for M7.0 scenario earthquake. Earthquake Spectra 23 (1), 95–113.

Petersen, M.D., Frankel, A.D., Harmsen, S.C., Mueller, C.S., Haller, K.M., Wheeler, R.L., Wesson, R.L., Zeng, Y., Boyd, O.S., Perkins, D.M., Luco, N., 2008. Documentation for the 2008 Update of the United States National Seismic Hazard Maps (No. 2008–1128). Geological Survey (US).

Rashidian, V., Gillins, D.T., 2018. Modification of the liquefaction potential index to consider the topography in Christchurch, New Zealand. Eng. Geol. 232, 68–81.

Rauch, A.F., Martin, J.R., 2000. EPOLLS model for predicting average displacements on lateral spreads. J. Geotech. Geoenviron. Eng. ASCE 126 (4), 360–371.

Saygili, G., Rathje, E.M., 2008. Empirical predictive models for earthquake-induced sliding displacements of slopes. J. Geotech. Geoenviron. Eng. 134 (6), 790–803.

Seed, H.B., 1979. Soil liquefaction and cyclic mobility evaluation for level ground during earthquakes. J. Geotech. Eng. Div. 105 (2), 201–255.

Seid-Karbasi, M., Byrne, P.M., 2007. Seismic liquefaction, lateral spreading and flow slides: a numerical investigation into void redistribution. Can. Geotech. J. 44 (7), 873–890.

Sharifi-Mood, M., 2017a. Probabilistic Geospatial Analyses, Uncertainty Modeling, and Mapping of Seismically-induced Ground Failures (Ph.D. Dissertation). Oregon State University, Corvallis. http://ir.library.oregonstate.edu/concern/graduate_thesis_or_dissertations/x059cd09j.

Sharifi-Mood, M., Olsen, M.J., Gillins, D.T., Mahalingam, R., 2017b. Performance-based, seismically-induced landslide hazard mapping of Western Oregon. Soil Dynamics and Earthquake Engineering 103, 38–54.

Sonmez, H., Gokceoglu, C., 2005. A liquefaction severity index suggested for engineering practice. Environ. Geol. 48 (1), 81–91.

Stewart, J.P., Afshari, K., Hashash, Y.M., 2014. Guidelines for performing hazard-consistent one-dimensional ground response analysis for ground motion prediction. In: PEER Report 2014/16, Pacific Earthquake Engineering Research Center, Berkeley, CA.

Ulmer, K., Ekstrom, L., Franke, K., 2015. Optimum grid spacing for simplified performance-based liquefaction and lateral spread displacement parameter maps. In: Proc. 6th International Conference on Earthquake Geotechnical Engineering, Nov 1. Christchurch, New Zealand.

Youd, T.L., Hoose, S.N., 1977. Liquefaction susceptibility and geologic setting. In: Proc., 6th World Conf. on Earthquake Engineering Vol. 6. Indian Society of Earthquake Technology, Roorkee, India, pp. 37–42.

Youd, T.L., Perkins, D.M., 1978. Mapping liquefaction-induced ground failure potential. J. Geotech. Eng. Div. 104 (GT4), 433–446.

Youd, T.L., Perkins, D.M., 1987. Mapping of liquefaction severity index. J. Geotech. Eng. 113 (11), 1374–1392.

Youd, T.L., Idriss, I.M., Andrus, R.D., Arango, I., Castro, G., Christian, J.T., Dobry, R., Finn, W.L., Harder Jr., L.F., Hynes, M.E., Ishihara, K., 2001. Liquefaction resistance of

soils: summary report from the 1996 NCEER and 1998 NCEER/NSF workshops on evaluation of liquefaction resistance of soils. J. Geotech. Geoenviron. 127 (10), 817–833.
Youd, T.L., Hansen, C.M., Bartlett, S.F., 2002. Revised multilinear regression equations for prediction of lateral spread displacement. J. Geotech. Geoenviron. Eng. 128 (12), 1007–1017.
Zhang, G., Robertson, P.K., Brachman, R.W., 2004. Estimating liquefaction-induced lateral displacements using the standard penetration test or cone penetration test. J. Geotech. Geoenviron. Eng. 130 (8), 861–871.